Teleoperation of a Mobile Robot Using a Force-Reflection Joystick With Sensing Mechanism of Rotating Magnetic Field

Seung Keun Cho, Hong Zhe Jin, Jang Myung Lee, *Senior Member, IEEE*, and Bin Yao, *Member, IEEE*

***Abstract*—Operators' intelligent and skillful decisions are necessary for the teleoperation of a mobile robot when there are many scattered obstacles. Among the sensors used for environment recognition, the camera is the most popular and powerful. However, there are several limitations in the camera-based teleoperation of a mobile robot. For example, shadowed and curved areas cannot be viewed using a narrow view-angle camera, especially in an environment with bad illumination and several obstacles. Therefore, it is necessary to have other sensory information for reliable teleoperations. In this study, 16 ultrasonic sensors are attached around a mobile robot in a ring pattern to measure the distances to the obstacles and a collision vector is introduced as a new tool for obstacle avoidance, which is defined as the normal vector from an obstacle to the mobile robot. Based on this collision vector, a virtual reflection force is generated to avoid the obstacles and then the reflection force is transferred to the operator who is holding the joystick used to control the mobile robot. Based on this reflection force, the operator can control the mobile robot more smoothly and safely. For this bidirectional teleoperation, a master joystick system using a two-axis hall sensor was designed to eliminate the nonlinear region, which exists in a general joystick with two motors and potentiometers. The effectiveness of the collision vector and force-reflection joystick is verified by comparing two vision-based teleoperation experiments, with and without force reflection.**

***Index Terms*—Hall sensor, haptic interface, joystick, mobile robot, teleoperation.**

I. Introduction

ROBOTS are beginning to be employed to replace human workers in dangerous and difficult situations. With the development of IT technologies, the technical concept of the robot has been extended to various applications, such as home appliances and recreation. In factory applications of mobile robots, painted lines or optical tapes combined with charge-coupled device (CCD) cameras and magnetic sensors are often used, with the robot following the fixed tracks repeatedly [1]. These factory robots can have precise tracking capabilities with high reliability, since they are required to follow a fixed track at all times. However, the installation of fixed tracks is not possible for service robots, surveillance robots, or cleaning robots, for which flexible and robust localization systems are required [2], [3].

In service robot applications, an autonomous system may not offer a sufficient degree of reliability, especially for dangerous and unexpected situations where highly intelligent decisions are required dynamically. Instead, a teleoperated control system where a human operator directly controls the robot according to his own decisions is more effective and reliable [4]. In conventional teleoperated systems, the operator relies mostly on visual information to control the slave robot, which has several shortcomings such as narrow viewing angles and environment-dependent resolutions [5], [6].

In this research, a bidirectional teleoperation system is proposed, where a slave robot receives the operator's commands through a joystick and sends back the environment information to the operator in the form of a feedback force. In the generation of the feedback force corresponding to the environment, a collision vector is newly defined to determine the direction of the reflection force required to avoid the obstacle. The reflection force is sent to the 2-DOF joystick to make the operator feel the force and manipulate the joystick accordingly [7], [8]. Since the collision vector is defined as the shortest normal vector from an obstacle to the mobile robot, it improves the collision avoidance efficiency obtained with a virtual impedance algorithm.

The joystick used for this research has a two-axis hall sensor instead of potentiometers to detect the joystick-bar displacements. Using this new structure, the joystick becomes free from the weariness associated with the friction between the bar and the housing and its position sensing performance is stabilized. This design's main improvement is that the joystick bar is constantly revolving around a universal joint and pointing to its center. This simple structure eliminates framework friction and solves the problem of performance degradation. It also has better performance than the conventional dual hall sensor or potentiometer structure, both which suffer from nonlinear characteristics due to their complex mechanisms [9]. Recent researches on force-reflection algorithms are well surveyed in [10], and the trajectory tracking and obstacles avoidance issue is introduced in an intelligent space [11].

In Section II, sensing mechanism of rotating magnetic field is introduced and, in Section III, the teleoperated control system is described systematically. The collision vector and virtual impedance algorithms, which are the main contribution of this paper, are introduced in Section IV. In Section V, experiments are performed to demonstrate the autonomous navigation and teleoperation of a mobile robot using the proposed algorithm,

Manuscript received May 15, 2008; revised November 8, 2008. First published March 4, 2009; current version published November 18, 2009. Recommended by Technical Editor H. Hashimoto. This work was supported by Korea Science and Engineering Foundation (KOSEF) Grant R01-2007-000-10171-0 funded by the Korea Government (MOST).

S. K. Cho and H. Z. Jin are with Pusan National University, Busan 609-735 Korea (e-mail: skcho2004@pusan.ac.kr; hit_pnu@pusan.ac.kr).

J. M. Lee is with Pusan National University, Busan 609-735 Korea, and also with the School of Mechanical Engineering, Purdue University, West Lafayette, IN 47907 USA (e-mail: jmlee@pusan.ac.kr).

B. Yao is with the School of Mechanical Engineering, Purdue University, West Lafayette, IN 47907 USA (e-mail: byao@ecn.purdue.edu).

Color versions of one or more of the figures in this paper are available online at http://ieeexplore.ieee.org.

Digital Object Identifier 10.1109/TMECH.2009.2013848

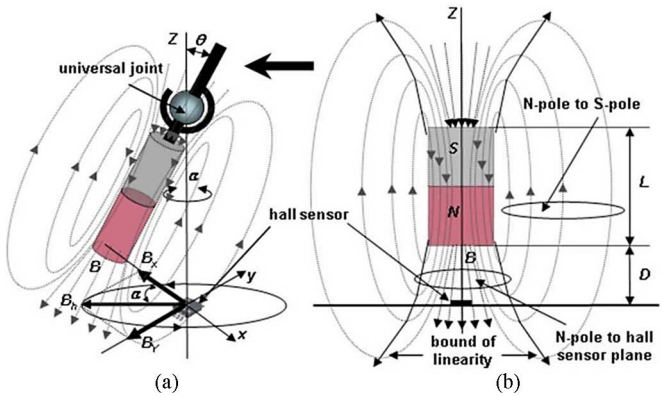

Fig. 1. Mechanical structure of the proposed joystick. (a) Shape of proposed joystick. (b) Sensing mechanism of magnetic flux lines.

and the results are analyzed to show its effectiveness. Section VI summarizes the contributions of this paper.

II. Sensing Mechanism of Rotating Magnetic Field

There is a universal joint in the rotation center of the joystick bar, which is the most important characteristic in this new structural design. This joint is different from the previous designs, as shown in Fig. 1(a). When the permanent magnet is reoriented with the universal joint by θ, the magnetic field $\vec{B}$ is projected onto the hall-sensor plane. This horizontal vector of the magnetic field $\vec{B}_h$ is resolved along the X and Y axes and is individually measured by the hall sensor. Fig. 1(b) shows the distribution of the magnetic field lines of the permanent magnet. The magnetic field lines out of the magnet bar run from the N-pole to the S-pole in a football-like shape. In other words, the directions of the magnetic field lines coming into and coming out of the magnet bar are in opposite directions. Also, the magnetic field lines are more sparsely spaced the farther they are from the center of the magnet bar. The intensity also weakens as it gets further away.

As shown in Fig. 1(b), the magnetic flux lines are running toward the hall sensor. The hall-sensor output is linear when the joystick bar moves within a certain bounded region where the hall sensor is mainly surrounded by the magnetic field lines from the N-pole to the hall-sensor plane. However, with the increase in the tilt angle θ the hall sensor is also influenced by the magnetic field lines returning to the S-pole from the N-pole, which causes the hall-sensor output corresponding to the joystick-bar motion around the universal joint to be highly nonlinear.

The relation between the magnetic flux density B and the corresponding horizontal vector B_h can be modeled as

$$B_h = \lambda(\theta)B \tag{1}$$

where $\lambda(\theta)$ incorporates the nonlinearities. When the magnetic flux lines are ideally parallel to the joystick bar, $\lambda(\theta)$ equals 1. However, in reality, the horizontal magnetic field does not increase linearly with an increase in the tilt angle θ. It actually decreases adversely in a certain range of the tilt angle. The nonlinear characteristics depend on the geometric shape, especially the length of the permanent magnet L, and the vertical distance between the permanent magnet-bar tip and hall sensor D.

To compensate for the nonlinearities, the nonlinear function $\lambda(\theta)$ is expressed as a function of θ in previous research [9] as

$$\lambda(\theta) = \frac{\sin(\theta)}{[1+(k\theta)^n]D^2} \tag{2}$$

where n is the linearity relationship between $\sin(\theta)$ and the hall-sensor output and k is a constant, which relates to the geometric shape of the magnet bar and the design specification of the joystick frame. The idea for (2) is derived from the observation that the experimental hall-sensor output is very similar to the frequency response of a low-pass filter.

The relation between the output voltages of the hall sensor (V_x, V_y) and the magnetic flux (B_x, B_y) is linear and is described as

$$\begin{aligned} V_x &= cB_x = cB_h\cos(\alpha) \\ V_y &= cB_y = cB_h\sin(\alpha) \end{aligned} \tag{3}$$

where the amplification factor c depends on the electrical constant of the hall sensor and the amplification factor of the signal transformation circuit and α is the rotation angle of the joystick bar.

After the amplification, low-pass filtering, and offset elimination, the hall-sensor output is converted to a digital signal by an A/D converter, which is computed in a digital signal processor (DSpic). If we combine (1), (2), and (3), the A/D converter outputs are

$$\begin{aligned} \mathrm{AD}_x &= \frac{(2^N-1)V_x}{V_{\mathrm{ref}}} = \xi\frac{\sin(\theta)}{1+(k\theta)^n}\cos(\alpha) \\ \mathrm{AD}_y &= \frac{(2^N-1)V_y}{V_{\mathrm{ref}}} = \xi\frac{\sin(\theta)}{1+(k\theta)^n}\sin(\alpha) \end{aligned} \tag{4}$$

where V_{ref} is the conversion range of the A/D converter, N represents the A/D converter resolution in bits, and the amplification factor of the A/D converter ξ is defined as

$$\zeta = \frac{c(2^N-1)B}{D^2V_{\mathrm{ref}}}. \tag{5}$$

And also, the rotation angle α on the X–Y plane can be determined as

$$\alpha = \tan^{-1}(V_y/V_x) = \tan^{-1}(\mathrm{AD}_y/\mathrm{AD}_x). \tag{6}$$

Note that AD_x and AD_y are proportional to the magnetic flux B and are also proportional to the square inverse of the distance D [12], [13].

In the universal joint joystick, the movement of the joystick bar is revealed by a 2-D flux vector on the hall-sensor plane, which is transformed by the hall sensor into the position values AD_x and AD_y. However, from (4), the A/D converted value of the hall-sensor output is not proportional to $\sin(\theta)$ owing to magnetic interferences. In other words, the relation between the hall-sensor output and the joystick-bar displacement is nonlinear. Therefore, a nonlinear compensation processing should be

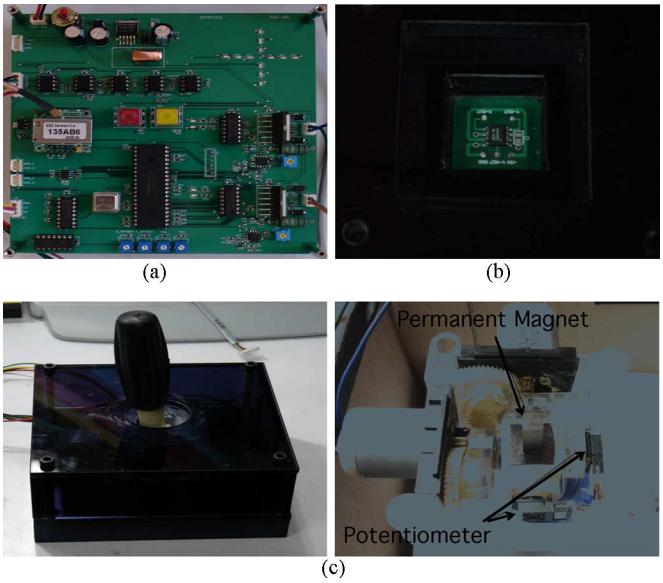

Fig. 2. Master joystick system. (a) Control board. (b) Hall sensor. (c) Structure of the joystick.

performed to precisely represent the displacement of the joystick bar. From (3) and (4), the composed output values of the voltages (V_x, V_y) and the A/D converter output are obtained as

$$V_c = \pm\sqrt{V_x^2 + V_y^2} = \frac{\xi V_{\text{ref}}}{2^N - 1} \times \frac{\sin(\theta)}{1 + (k\theta)^n} \tag{7}$$

$$\text{AD}_c = \pm\sqrt{\text{AD}_x^2 + \text{AD}_y^2} = \xi \frac{\sin(\theta)}{1 + (k\theta)^n}. \tag{8}$$

Due to the limitation of this paper, the solution of θ is directly quoted as follows [9]:

$$\theta_{i+1} = \theta_i + \frac{\text{AD}_c k^{2n} \theta_i^{2n} + [2\text{AD}_c - \xi \sin(\theta_i)] k^n \theta_i^n + [\text{AD}_c - \xi \sin(\theta_i)]}{[k^n \xi \cos(\theta_i)]\theta_i^n - [nk^n \xi \sin(\theta_i)]\theta_i^{n-1} + \xi \cos(\theta_i)}. \tag{9}$$

The result of (9) is derived from the Newton method for solving a nonlinear equation, and i represents the recursive number. In the experimental study, the maximum recursive number is set as 7. Based on observation of the experimental results, this value sufficiently guarantees the real-time performance.

From (6) and (9), the command of the linearized position vector $V_h = \gamma \cdot l \cdot \sin(\theta)$ (γ: scaling constant, l: length of joystick bar) and the orientation α can be obtained in order to assure the teleoperation of the robot. The joystick system is illustrated in Fig. 2 where (a) shows the control board, (b) the hall sensor, and (c) the structure.

The permanent magnet of the joystick is made of Alnico materials and has an intensity of 1800–2000 Gauss. For the hall sensor, a 2 SA-10 sensor from Sentron Corporation, Switzerland, was selected for the experiments. The vertical distance between the permanent magnet and hall sensor D is 13 mm, and the total length of the joystick bar is 31 mm. The

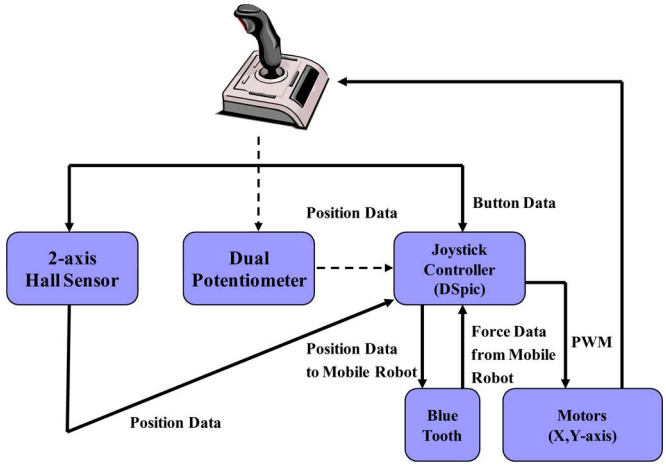

Fig. 3. Functional block diagram of the joystick.

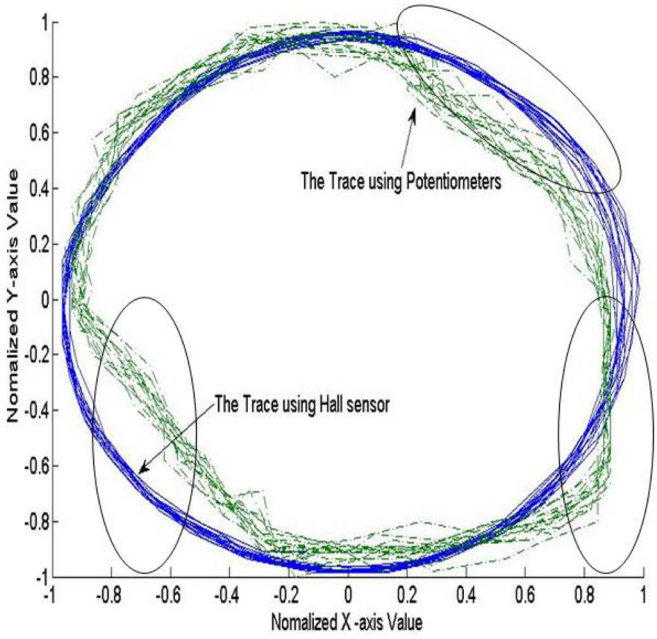

Fig. 4. Performance comparison between the two types of joysticks.

conventional joystick used in this experiment for comparison has a 100 kΩ potentiometer at each motor axis.

The functional block diagram of the joystick is shown in Fig. 3. The controller for the joystick is implemented with a DSpic microprocessor, which controls the dc motors using the pulsewidth modulation (PWM) voltage output to make the operator feel the reflected force corresponding to the virtual force (F_x, F_y) sent from the mobile robot. L6203 drivers are used to drive the dc motors.

Fig. 4 represents the traces of a 15-turn circular motion measured by the two-axis hall sensor and dual potentiometer joysticks, respectively. As shown in Fig. 4, the trace using the hall sensor is nearly a round circle. However, the trace using the potentiometer has nonlinear characteristics in several regions and the motion ranges along the x- and y-axes are normalized as -1 to 1.

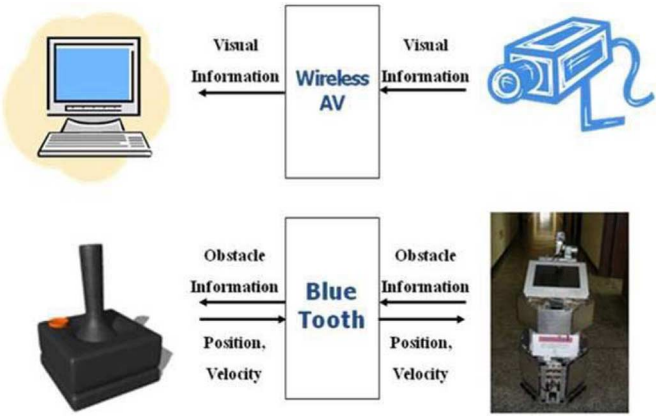

Fig. 5. Overall system block diagram.

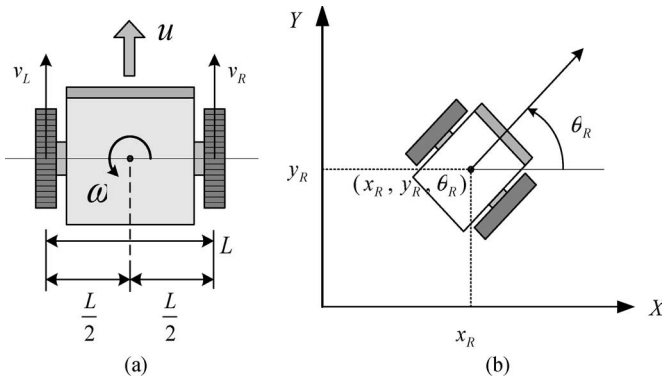

Fig. 6. Mobile robot model.

III. Teleoperated Control System

A. Teleoperated Control

The teleoperated control system proposed in this paper consists of a master joystick, a slave mobile robot, and a Bluetooth (max. 100 m) and wireless AV transceiver (max. 50 m) for communication (refer to Fig. 5). When the operator moves the joystick, the joystick controller transmits the corresponding velocity and orientation command to the mobile robot. According to these commands that the mobile robot receives, it implements the proper speed control.

While the mobile robot is moving, the ultrasonic sensors attached around the robot gather environmental information in the form of the reflection force against obstacles and send the information back to the operator, who can then feel the force [8], [14], [15].

In summary, the mobile robot follows the velocity commands from the operator, detects obstacles, and transmits the obstacle information back to the operator. Therefore, the operator can implement telepresence through the feedback force, which is proportional to the distance and relative velocity between the mobile robot and obstacles [16], [17].

B. Slave Mobile Robot

To analyze the motion of the mobile robot, the world and robot coordinates are defined in 2-D space, as shown in Fig. 6, where the position and orientation vector can be represented as $P = [x\ y\ \theta]^T$.

Notice that the motion of the mobile robot can be described by the linear velocity u and the angular velocity ω and that they are functions of the velocities of the left and right wheels v_L and v_R

$$u = \frac{1}{2}(v_R + v_L) \tag{10}$$

$$\omega = \frac{1}{L}(v_R - v_L). \tag{11}$$

The velocity $\dot{P}$ in the world coordinates is related to the input variable q by the Jacobian matrix as follows:

$$\dot{P} = J(p)\,\dot{q} \tag{12}$$

where $\dot{P} = \begin{bmatrix}\dot{x} & \dot{y} & \dot{\theta}\end{bmatrix}^T \in R^n$, $\dot{q} = [u \quad \omega]^T \in R^m$

$$J(P) = \begin{bmatrix}\cos\theta & 0\\ \sin\theta & 0\\ 0 & 1\end{bmatrix}$$

and n and m are the dimensions of the world coordinates systems and local robot coordinate system, respectively. Note that here n is 3 and m is 2.

The position vector P in the world coordinates systems can be obtained using the integration of (12) as

$$P = \begin{bmatrix}x\\ y\\ \theta\end{bmatrix} = \begin{bmatrix}x_0\\ y_0\\ \theta_0\end{bmatrix} + \begin{bmatrix}\int u(\tau)\cos(\theta(\tau))d\tau\\ \int u(\tau)\sin(\theta(\tau))d\tau\\ \int \omega(\tau)d\tau\end{bmatrix}. \tag{13}$$

Using these geometrical relations, the position of the mobile robot can be calculated at every control cycle, while u and ω are calculated using the wheel encoders.

Based on the kinematic relationships in (10) and (11), the speed command of the left and right wheel is distributed according to the following rules:

$$v_{rc} = u_c + \frac{\omega L}{2} \tag{14}$$

$$v_{lc} = u_c - \frac{\omega L}{2} \tag{15}$$

where v_{rc}, v_{lc}, and u_c correspond to v_R, v_L, and u, respectively, and u_c is obtained from the joystick controller, which is proportional to V_h. In (14) and (15), the rotation angular velocity ω is equal to $\dot{\alpha}$.

The experimental mobile robot incorporates a CCD camera on the top, 16 ultrasonic sensors around the body, and two dc motors/encoders at the bottom. Basically, two differential motors are used to drive the mobile robot and the two passive wheels placed in front and behind the robot enable it to keep its balance. To keep the wheels on the surface and minimize slippage, springs are used in the passive wheels. The motor specifications for the driving wheels are 24 V, 40 W, 0.8 A, 300 r/min (after 10:1 reduction), and 80 kgf/cm torque outputs (S8D40-24 A). The encoder attached to the motor is utilized for velocity control and for position calculation.

Fig. 7. Picture of the experimental robot.

Fig. 7 shows a picture of the experimental robot. There are 16 SRF04 ultrasonic sensors attached around the mobile robot, and the detecting range of the sensors extends from a minimum of 0.03 m to a maximum of 3 m. To reduce the interference among the sensors, each sensor is allowed to work only in a certain period of time through a decoder and a multiplexer. Encoders are utilized to control the wheel velocities of the mobile robot. Therefore, the position vector of the navigating mobile robot is calculated at each control period of the wheel. The encoder accuracy 360 [pulse/rev] is improved by four times to 1440 [pulse/rev] by using an LS7166.

IV. Reflection of a Virtual Force

The virtual impedance method is a modification of the general impedance algorithm for mobile robot navigation and the collision avoidance of obstacles [16], [18], [19]. As illustrated in Fig. 8, the relation between the mobile robot and its goal position/obstacles is modeled by springs and dampers. Based on the virtual impedance model, the feedback force is calculated and transmitted to the joystick to reflect the environmental situations by the force and torque.

The virtual force to be sent to the operator F_b is calculated to incorporate static obstacles as well as dynamic obstacles as

$$F_b = \sum_{i=0}^{n_s} F_{\rm os}\,(i) + \sum_{i=0}^{n_d} F_{\rm od}\,(i) \tag{16}$$

where n_s and n_d are the numbers of static and dynamic obstacles, respectively, and $F_{\rm os}$ and $F_{\rm od}$ are computed using the

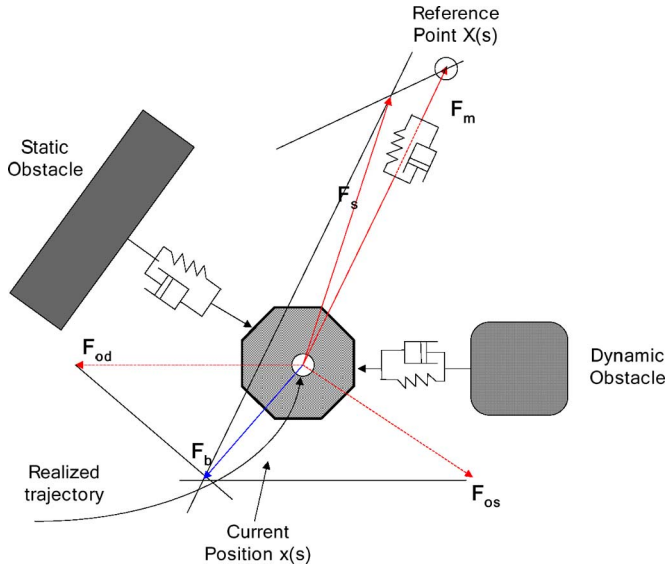

Fig. 8. Virtual impedance model.

following virtual impedance model:

$$F_{\rm os}(i) = K_{s,i}\cdot X_s(i) + D_{s,i}\cdot \dot{X}_s(i)$$
$$= \begin{cases} K_{s,i}\cdot(\rho_0 - \|\overrightarrow{C_i}\|)\overrightarrow{C}_{i,\rm unit} & \in \text{when } \|\overrightarrow{C_i}\|<\rho_0 \\ -D_{s,i}\cdot(\Delta\|\overrightarrow{C_i}\|)\overrightarrow{C}_{i,\rm unit,} & \\ 0 & \text{otherwise} \end{cases} \tag{17}$$

where ρ_0 (85 cm) represents the threshold for collision avoidance and should be kept smaller than the sensible range of the ultrasonic sensors 3 m, the collision vector $\vec{C}_i$ is defined as a normal vector from an obstacle to the mobile robot, $\vec{C}_{i,\rm unit}$ is its unit vector, and $\Delta\vec{C}_i$ is defined as the difference between the current and previous collision vectors. Also, $K_{s,i}$ is a spring coefficient and $D_{s,i}$ is a damper coefficient of the virtual impedance model. The value of $F_{\rm od}$ can be obtained by replacing "s" to "d" in (17).

The attraction force to the goal F_m in Fig. 8 is generated by the operator who is monitoring and controlling the mobile robot by means of the joystick in this approach. The virtual force generated for obstacle avoidance has the same form as that in the case of the general impedance algorithm. However, a collision vector is newly introduced in this paper to define the direction of the virtual spring, as well as the virtual damper, as the variation of the collision vector, which improves the collision avoidance performance dramatically. When the virtual impedance algorithm is applied for obstacle avoidance, the mobile robot stops near obstacles and/or moves very slowly in between obstacles with some chattering. With the aid of this collision vector, the mobile robot changes its course to avoid rapidly approaching obstacles and keeps closely to the planned path after collision avoidance.

Since the ultrasonic sensor has its own sensitivity range, usually about $\pm 22.5^\circ$, obstacles located at an angle of more than 30° from the center of the sensor beam cannot be detected

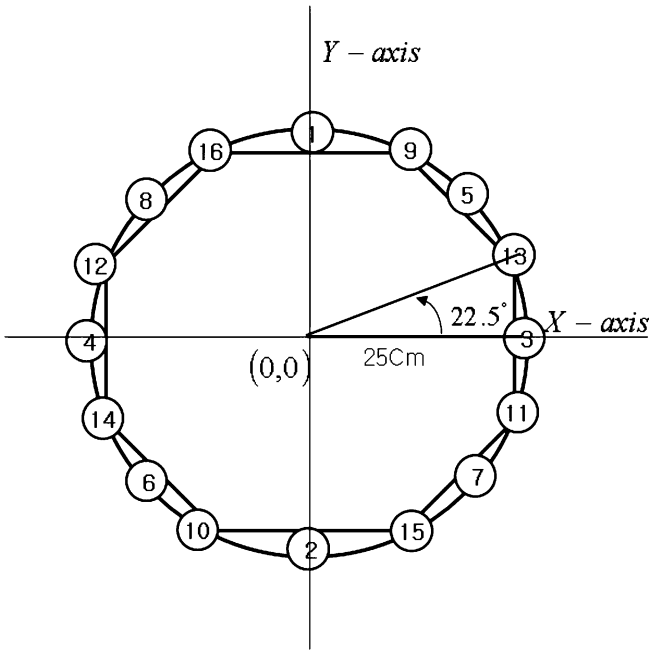

Fig. 9. Arrangement of the ultra sonic sensors.

reliably. Sixteen ultrasonic sensors are installed around the mobile robot, meaning there is a sensor every 22.5°. Refer to Fig. 9.

Therefore, there are only three reliable ultrasonic sensors at a certain instant, which can be used to measure the distance from the mobile robot to the obstacle. Based on this observation, the types of obstacles that can be detected by the mobile robot are classified into three categories: 1) Small obstacles that can only be detected by a single ultrasonic sensor, such as human beings or small trash cans; 2) Slightly larger obstacles detected by two ultrasonic sensors, such as a large box or table; and 3) Long obstacles detected by three sensors, such as a wall or a long table (refer to Fig. 10(a), (b), and (c), respectively).

1) In the first case, the collision vector can be obtained directly from the measured distance vector, as shown in Fig. 10(a), and it is represented as

$$\vec{C} = \vec{L}_{\min}. \tag{18}$$

2) In the second case, the shorter distance vector is denoted as $\vec{L}_1$ and the other as $\vec{L}_2$ [refer to Fig. 10(b)]. A normal vector, which is defined as a collision vector, to the center of the mobile robot can be found on the line connecting the two points P_1 and P_2, which can be calculated as

$$P_1 = (x_1, y_1) = (d_1 \cos\theta_1, d_1 \sin\theta_1) \tag{19}$$

$$P_2 = (x_2, y_2) = (d_2 \cos\theta_2, d_2 \sin\theta_2) \tag{20}$$

where d_1 and d_2 represent the distances from the mobile robot to the points P_1 and P_2 and θ_1 and θ_2 represent the angles to points P_1 and P_2 from the mobile robot, respectively. Now the collision vector point on the obstacle

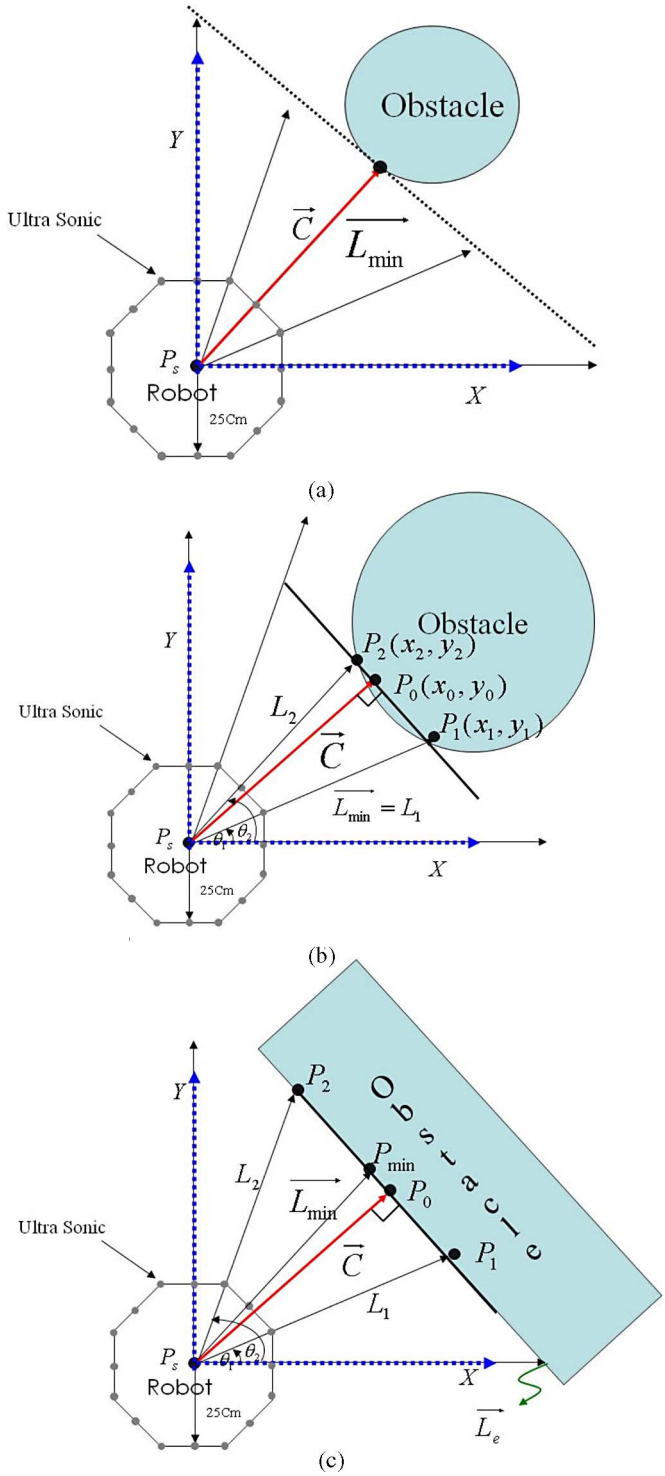

Fig. 10. Determination of the collision vector for three different types of obstacles. (a) Case 1. (b) Case 2. (c) Case 3.

P_0 can be calculated as

$$P_0 = (x_0, y_0) = \left(\frac{S \cdot x_1 - y_1}{S + 1/S}, \frac{-x_1 + 1/S \cdot y_1}{S + 1/S} \right) \tag{21}$$

$$\vec{C} = \overrightarrow{P_0 P_s} \tag{22}$$

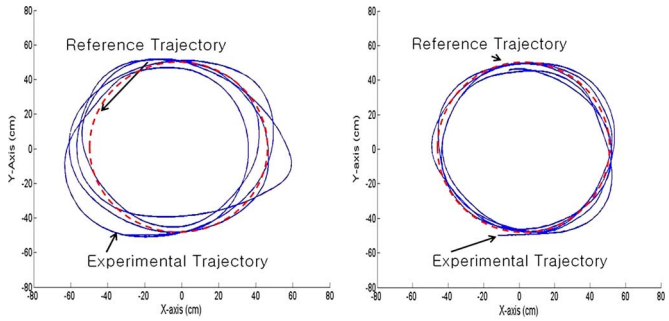

Fig. 11. Robot trajectory comparison. (a) Using the potentiometer joystick. (b) Using the hall-sensor joystick.

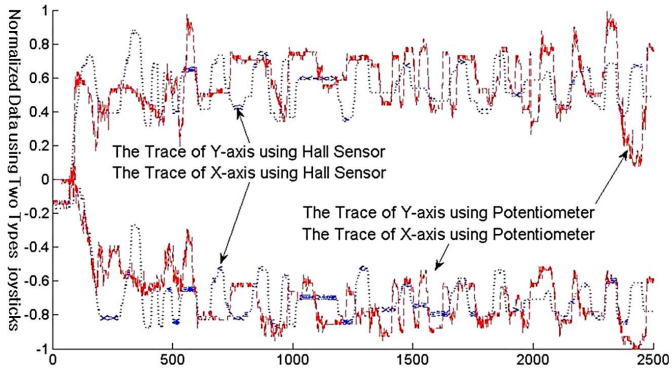

Fig. 12. Trace error comparison of the two types of joysticks.

where $S = \frac{y_2 - y_1}{x_2 - x_1}$, P_s represents the current position of the mobile robot, and θ represents the angle between the motion direction of the mobile robot X_R, and the beam center of the ultrasonic sensor.

3) In the last case, the shortest of the three vectors is denoted as $\vec{L}_{\min}$, the right vector is denoted as $\vec{L}_1$, and the last vector as $\vec{L}_2$. The two vectors $\vec{L}_{\min}$ and $\vec{L}_1$ can be used to define the collision vector, like the second case. Note that $\vec{L}_e$ is ignored since its angle with $\vec{C}$ is greater than 30°.

The generated virtual force F_b at the slave mobile robot is transmitted to the operator and is transformed into the rotational force as

$$\tau_b(s) = \text{sat}(K_b \cdot F_b(s)) \tag{23}$$

where

$$\text{sat}(x) = \begin{cases} x, & \text{if } |x| \le x_{\max} \\ \text{sgn}(x) \cdot x_{\max}, & \text{otherwise} \end{cases}$$

and K_b represents the force feedback gain.

Now the operator can feel the distance to an obstacle through the reflected force τ_b on the joystick, which enables him to drive the mobile robot safely, even under the constraint of limited visual information.

V. Experiments and Results

Three experiments were performed individually. The first experiment compares the performances of a mobile robot controlled by the joystick with a two-axis hall sensor and potentiometers. The second experiment shows the collision vectors according to Fig. 10(a)–(c) and reveals the reflective force at each x- and y-axis of the joystick as a current value. The last experiment demonstrates the feedback force measured by the force/torque sensor while a mobile robot is navigating in an environment with obstacles under the control of the joystick with a two-axis hall sensor.

In Fig. 11, the red dotted circle is a reference trajectory whose radius is 50 cm. Fig. 11(a) shows the traces of the mobile robot controlled by the joystick with potentiometers and (b) shows the traces by the joystick with the hall sensor. It is very clear that the joystick with the hall sensor provides high accuracy in its control by providing reliable positional variation data (refer to Fig. 12).

In the second experiment, the three types of obstacles in Fig. 10(a)–(c) are placed in front of the mobile robot one by one.

When ultrasonic sensor five detects an obstacle as in the case of Fig. 10(a), the obstacle's orientation can be identified as 45° with respect to. the x-axis of the local robot coordinate system (refer to Fig. 9).

The reflective force is calculated by (17) of the virtual impedance algorithm, and this force can be decomposed into repulsive Force_x and repulsive Force_y ($\theta = 45^\circ$)

$$\begin{aligned} \text{Repulsive Force\_}x &= -1 \times (\text{Force} \times \cos(\theta)) \\ \text{Repulsive Force\_}y &= -1 \times (\text{Force} \times \sin(\theta)) \end{aligned} \tag{24}$$

where the negative sign is placed for the joystick actuators and the current flow proportional to the repulsive forces is determined with the collision vector. For the experiment, the speed of the mobile robot is kept at 10 cm/s and the optimal values for K_s and D_s in (17) are empirically selected as 7 N/m and 11 N/m·s, respectively. Fig. 13(a) illustrates the repulsive force and the corresponding current.

For the next two experiments corresponding to the cases of Fig. 10(b) and (c), the obstacle is located in front of the mobile robot. Depending on the size of the obstacle, ultrasonic sensors 9 and 1 ($\theta_1 = 67.5^\circ$, $\theta_2 = 90^\circ$) detect the obstacle and ultrasonic sensors 16, 1, and 9 ($\theta_1 = 67.5^\circ$, $\theta_2 = 112.5^\circ$) detect the obstacle. For these cases, the repulsive force is also decomposed into two components:

$$\begin{aligned} \text{Repulsive Force\_}x &= -1 \times (\text{Force} \times \cos((\theta_1 + \theta_2)/2)) \\ \text{Repulsive Force\_}y &= -1 \times (\text{Force} \times \sin((\theta_1 + \theta_2)/2)). \end{aligned} \tag{25}$$

Fig. 13(b) and (c) represent the repulsive force and corresponding current for the obstacle in cases 2 and 3, respectively.

Through the three obstacle experiments it is verified that the relation between the current at the actuator of the joystick and the repulsive force is linear even though there is a slight deviation. Therefore, the operator can feel the repulsive force at the joystick when the obstacle is closely approaching the mobile robot with a high speed, which makes the teleoperation with the force reflective joystick both precise and more reliable.

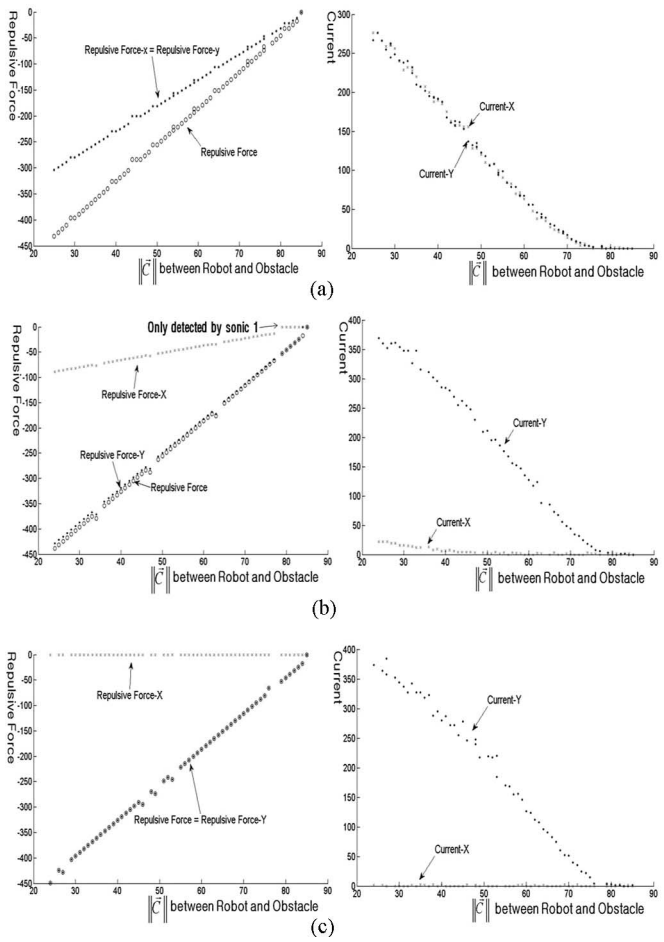

Fig. 13. Repulsive force and current about each case at Fig. 10. (a) Repulsive force and current for case 1. (b) Repulsive force and current for case 2. (c) Repulsive force and current for case 3.

Third experiment was performed to show the effectiveness of the force reflection for the guidance of the mobile robot in a dark environment. To emphasize the effects of using the force reflective joystick, the vision information from the CCD camera was deliberately limited by low illumination. Also, to verify the effectiveness of the collision vector for obstacle avoidance, the initial path planning for the mobile robot aims at the shortest distance as well as the shortest time to the goal. The navigation environment included seven static obstacles of triangular, cylindrical, and rectangular shapes, which could be detected by one, two, and three ultrasonic sensors, respectively. The three shapes are simplified models of trash cans, desks, computers, and people in their daily lives. The experimental environment was kept the same for the autonomous and teleoperated navigations.

A. Autonomous Navigation

It took 58 s for the mobile robot to navigate from the initial position to the target position using the virtual impedance algorithm with the newly defined collision vector in (17). In this autonomous mode, the attraction force F_m is predetermined empirically to minimize the traveling distance to the goal. The trace of the mobile robot measured by the encoders is illustrated in Fig. 14, where it is noted that the mobile robot navigates to the goal without colliding with the obstacles.

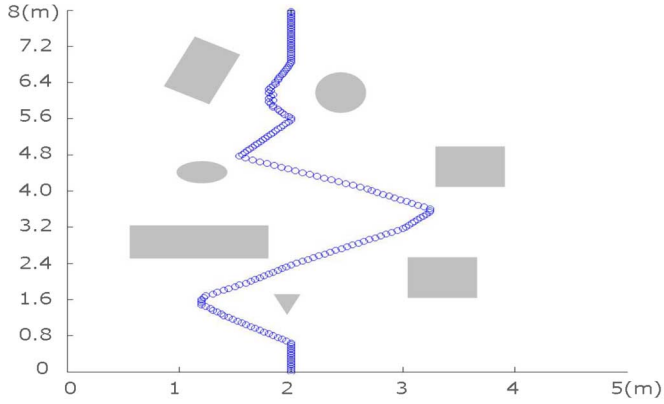

Fig. 14. Trace of the mobile robot in the autonomous navigation.

The joystick bar is stably grasped by a Scorobot ER-VII robot to measure the reflected force from the mobile robot in the autonomous navigation using an ATI-FT3186 force torque sensor attached at the wrist. Since the mobile robot is in autonomous mode, it does not receive any commands from the joystick during the navigation but simply feeds the reflection force based on the virtual impedance algorithm back to the joystick. This reflected force F_b is measured by the force torque sensor to show the coincidence between the virtual force and the actually reflected force in autonomous navigation. Fig. 15(a) represents the feedback force generated by the virtual impedance algorithm, (b) the measured force reflected back to the joystick (operator), and (c) the discrepancy between the previous two forces, which should be zero in an ideal system.

Through experimental analysis, it can be recognized that the error comes from the nonlinearities of the dc motors in the joystick. That is, when the duty ratio of the PWM signal to drive the motors is increased, the current flow in the motors is no longer linearly proportional to the PWM input. In the experiments, the error is kept below 5% by compensating the offset of the force/torque sensor and the nonlinearities of the motors properly.

B. Teleoperated Navigation

In the same environment as the autonomous navigation, two individual operators performed the teleoperation to drive the mobile robot to the goal position with and without the reflection force through the joystick.

In the first experiment, a CCD camera and a force-reflection joystick were used for teleoperation. Both the operators achieved the goal approximately 10 s faster than the autonomous navigation (operator A (48 s) and operator B (46 s) to the goal). The navigation traces are shown in Fig. 16. Note that the operators drove the mobile robot in a shorter course to the goal than the autonomous navigation, since they made partial use of vision information.

In the second experiment, the force feedback to the joystick is disconnected to show the effects of the force reflection. Vision

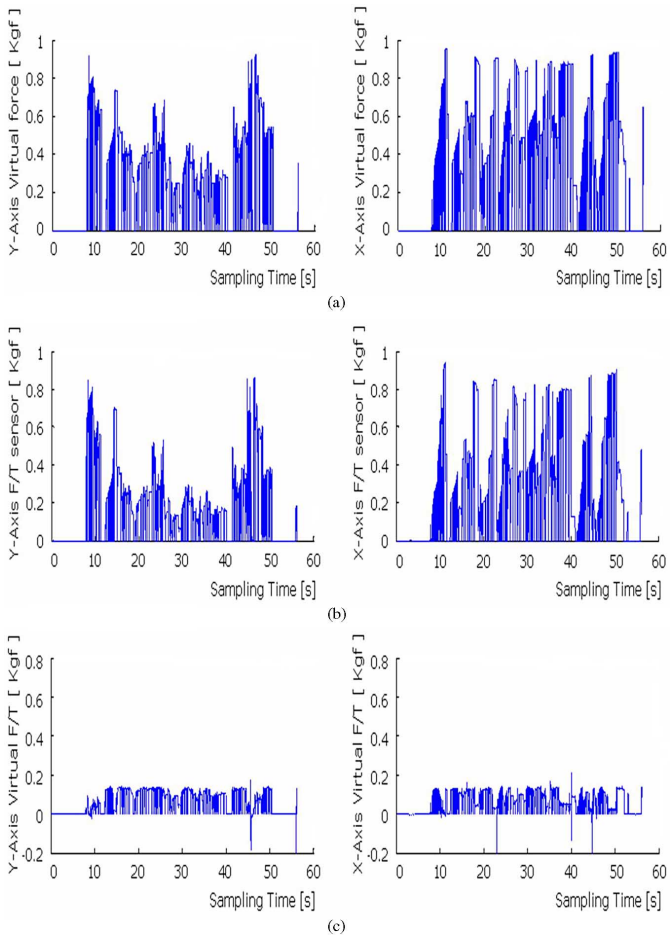

Fig. 15. Force/torque values during the autonomous navigation. (a) Virtual force data. (b) F/T sensor data. (c) Error in force reflection.

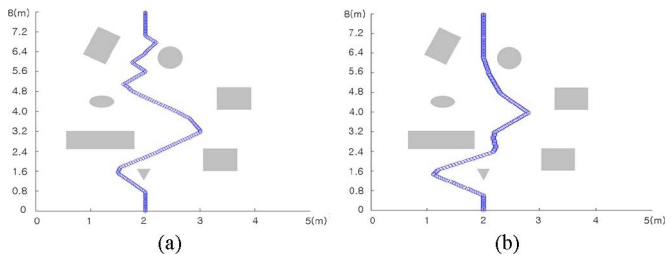

Fig. 16. Teleoperation of the mobile robot using force feedback. (a) Navigation trace of operator A. (b) Navigation trace of operator B.

information gathered under fairly low illumination is provided to the operator to drive the mobile robot.

As shown in Fig. 17, the operator cannot find a short course to the goal in the dark environment using only the CCD camera. Since he does not have any information on the distance between the mobile robot and the obstacles, he lets the mobile robot collide with the obstacles several times and follows a long course to the goal. The average teleoperated navigation time is 1 min and 20 s, which is 22 s longer than the autonomous navigation and 33 s longer than the teleoperation with force reflection.

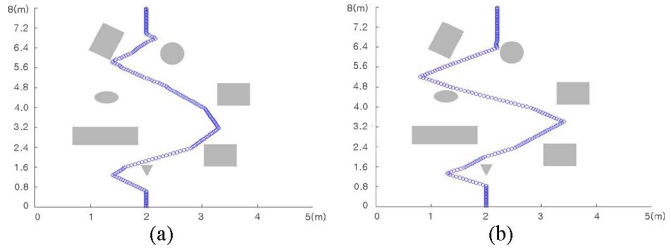

Fig. 17. Teleoperation of the mobile robot without force feedback. (a) Navigation trace of operator A. (b) Navigation trace of operator B.

VI. Conclusion

In this paper, a collision vector is newly introduced in the form of a normal vector from an obstacle to the mobile robot to improve the obstacle avoidance performance of the mobile robot under teleoperation as well as autonomous navigation.

The reflected force transmitted to the operator through the joystick is determined based on the modified virtual impedance algorithm, which uses the collision vector. To show the effects of the reflected force on the teleoperation of the robot, the reflected force of the joystick was measured by a six DOF sensor installed in the gripper. On account of the nonlinearities of the motors with respect to the PWM input, the measured value does not exactly match the virtual force calculated to avoid the obstacles. In the experiments, the error could be kept within 5%. The efficiency of obstacle avoidance was proven by comparing the results of two teleoperation experiments with and without the reflection force in the joystick. To emphasize the necessity for haptic feedback and to limit the usability of the camera, the experimental environment was kept dark. Through the analysis, it was shown that by using the joystick with haptic feedback, the operator can drive the mobile robot to the goal position much faster and more safely. As a part of this research, a single hall-sensor joystick was developed, which exhibits better linearity and durability than the conventional joystick. Therefore, this single hall-sensor joystick is expected to be popular for the teleoperation of mobile robots and precision machines with haptic feedback. The incorporation of motor nonlinearities and human hand dynamics in order to convey the environmental information to the operator more realistically is left as a future avenue of research, which is necessary for the mobile robot to navigate in the environment with random real-life shape obstacles on the irregular surface.

References

[1] J. Borenstein and Y. Koren, "Tele-autonomous guidance for mobile robots," *IEEE Trans. Syst., Man, Cybern.*, vol. 20, no. 6, pp. 1437–1443, Nov./Dec. 1990.

[2] D. Schulz, W. Burgard, D. Fox, S. Thrun, and A. B. Cremers, "Web interfaces for mobile robots in public places," *IEEE Robot. Autom. Mag.*, vol. 7, no. 1, pp. 48–56, Mar. 2000.

[3] C. R. Wagner and D. P. Perrin, "Force feedback in a three-dimension ultrasound guided surgical task," in *Proc. 14th Symp. Haptic Interfaces Virtual Environ. Teleoperator Syst.*, 2006, pp. 43–48.

[4] U. Tumerdem and K. Ohnishi, "Haptic consensus in bilateral teleoperation," in *Proc. 4th IEEE Int. Conf. Mechatronics (ICM 2007)*, May, pp. 1–6.

[5] S. S. Lee and J. M. Lee, "Haptic interface design for the tele-surgery," in *Proc. CIDAM Workshop Service Autom. Robot.*, Hong Kong, 2000, pp. 81–91.

[6] C. Basdogan, C.-H. Ho, and M. A. Srinivasan, "Virtual environments for medical training: Graphical and haptic simulation of laparoscopic common bile duct exploration," *IEEE/ASME Trans. Mechatronics*, vol. 6, no. 3, pp. 269–285, Sep. 2001.
[7] S. K. An, S. J. Han, H. R. Hur, and J. M. Lee, "Implementation of a remote peg-in-hole operation using a two degrees of freedom force-reflective joystick," *J. Electr. Eng. Inf. Sci.*, vol. 4, no. 3, pp. 315–322, 1999.
[8] J. Jayachandran, J. Gu, and J.-Y. Pan, "Teleoperation of a mobile robot using predictive control approach electrical and computer engineering," in *Proc. Can. Conf. CCECE 2006*, pp. 410–413.
[9] H. Z. Jin, H. Lu, S. K. Cho, and J. M. Lee, "Nonlinear compensation of a new noncontact joystick using the universal joint mechanism," *IEEE/ASME Trans. Mechatronics*, vol. 12, no. 5, pp. 549–556, Oct. 2007.
[10] I. G. Polushin, P. X. Liu, and C.-H. Lung, "A force-reflection algorithm for improved transparency in bilateral teleoperation with communication delay," *IEEE/ASME Trans. Mechatronics*, vol. 12, no. 3, pp. 361–374, Jun. 2007.
[11] C.-L. Hwang and L.-J. Chang, "Trajectory tracking and obstacle avoidance of car-like mobile robots in an intelligent space using mixed H_2/H_∞ decentralized control," *IEEE/ASME Trans. Mechatronics*, vol. 12, no. 3, pp. 345–352, Jun. 2007.
[12] "Angular position sensing measurement with SENTRON hall ASIC," SENTRON AG, Zug, Switzerland, Appl. Note 17, 2001.
[13] "2 SA-10, Integrated 2-axis Hall Sensor," SENTRON AG, Zug, Switzerland, Appl. Note, The Part of Linear Position Sensing and Joystick Application.
[14] I. G. Polushin, P. X Liu, and C.-H. Lung, "A force-reflection algorithm for improved transparency in bilateral teleoperation with communication delay," *IEEE/ASME Trans. Machatronics*, vol. 12, no. 3, pp. 361–374, Jun. 2007.
[15] R. C. Luo, C.-Y. Hu, T. M. Chen, and M.-H. Lin, "Force reflective feedback control for intelligent wheelchairs," in *Proc. IEEE/RSJ Int. Conf. (IROS 1999)*, vol. 2, pp. 918–923, Oct.
[16] S. S. Ge and Y. J. Cui, "New potential functions for mobile robot path planning," *IEEE Trans. Robot. Autom.*, vol. 16, no. 4, pp. 615–620, Oct. 2000.
[17] M. Nohmi, A. Ando, and T. Bock, "Contact task by space teleoperation using force reflection of communication time delay," in *Proc. IEEE Int. Symp. CIRA*, 2005, pp. 193–198.
[18] M. Ouhyung, W.-N. Tasi, and M.-C. Tsai, "A low-cost force feedback joystick and its use in PC video games," *IEEE Trans. Consum. Electron.*, vol. 41, no. 3, pp. 787–794, Aug. 1995.
[19] K. Kaneko, H. Tokashiki, K. Tanie, and K Komoriya, "Macro–micro bilateral teleoperation based on operational force feedforward-operational force feedforward bilateral teleoperation and its dexterity Intelligent Robots and Systems," in *Proc. 1998 IEEE/RSJ Int. Conf.,* Oct., vol. 3, pp. 1761–1769.

Seung Keun Cho received the B.S. degree in control engineering in 2004 from Pukyung National University, Busan, Korea, and the M.S. degree in electronic engineering in 2006 from Pusan National University, Busan, where he is currently working toward the Ph.D. degree in electronic engineering.

His current research interests include localization using ultrasonic sensor and haptic device using virtual impedance algorithm.

Hong Zhe Jin received the B.S. degree in measurement and control engineering in 1999 from Harbin Institute of Technology (HIT), Harbin, China, and the M.S. degree in electronic engineering in 2006 from Pusan National University, Busan, Korea, where he is currently working toward the Ph.D. degree in electronic engineering.

His current research interests include design, analysis, and control of nonlinear dynamical systems based on learning control theory and techniques of distributed sensor networks.

Jang Myung Lee (M'85–SM'03) received the B.S. and M.S. degrees in electronic engineering from Seoul National University, Seoul, Korea, in 1980 and 1982, respectively, and the Ph.D. degree in computer engineering from the University of Southern California (USC), Los Angeles, in 1990.

Since 1992, he has been a Professor with the Intelligent Robot Laboratory, Pusan National University, Busan, Korea, where he is also the Head of the Electrical Engineering School. His current research interests include intelligent robotic systems, transport robot, and intelligent sensors and control algorithms.

Prof. Lee was the former Chairman of the Research Institute of Computer Information and Communication. He is currently the Vice President of the Korean Robotics Society.

Bin Yao (S'92–M'96) received the B.Eng. degree in applied mechanics from Beijing University of Aeronautics and Astronautics, Beijing, China, in 1987, the M.Eng. degree in electrical engineering from Nanyang Technological University, Singapore, in 1992, and the Ph.D. degree in mechanical engineering from the University of California, Berkeley, in 1996.

Since 1996, he has been with the School of Mechanical Engineering, Purdue University, Lafayette, IN. He is also one of the Kuang-Piu Professors at Zhejiang University, Hangzhou, China. His current research interests include the design and control of intelligent high-performance coordinated control of electromechanical/hydraulic systems, optimal adaptive and robust control, nonlinear observer design and neural networks for virtual sensing, modeling, fault detection, diagnostics, adaptive fault-tolerant control, and data fusion.